RSC Advances

PAPER

View Article Online
View Journal | View Issue

Cite this: *RSC Adv.*, 2023, **13**, 26509

Self-assembled molybdenum disulfide nanoflowers regulated by lithium sulfate for high performance supercapacitors†

Yunan Li, *[ab] Yang Sun,[a] Sen Zhang,[a] Xueling Wu,[a] Meng Song,[a] Mingli Jiao,[a] Qi Qin*[a] and Liwei Mi *[b]

Received 19th July 2023
Accepted 31st August 2023

DOI: 10.1039/d3ra04852g

rsc.li/rsc-advances

Recently, molybdenum disulfide (MoS_2) has been extensively investigated as a promising pseudocapacitor electrode material. However, MoS_2 usually exhibits inferior rate capability and cyclability, which restrain its practical application in energy storage. In this work, MoS_2 nanoflowers regulated by Li_2SO_4 (L-MoS_2) are successfully fabricated *via* intercalating solvated Li ions. *Via* appropriate intercalation of Li_2SO_4, MoS_2 nanosheets could self-assemble to form L-MoS_2 nanoflowers with an interlayer spacing of 0.65 nm. Due to the large specific surface area (23.7 $m^2\ g^{-1}$) and high 1T phase content (77.5%), L-MoS_2 as supercapacitor electrode delivers a maximum specific capacitance of 356.7 F g^{-1} at 1 A g^{-1} and maintains 49.8% of capacitance retention at 20 A g^{-1}. Moreover, the assembled L-MoS_2 symmetric supercapacitor (SSC) device displays an energy density of 6.5 W h kg^{-1} and 79.6% of capacitance retention after 3000 cycles.

1. Introduction

Molybdenum disulfide (MoS_2), a typical two-dimensional (2D) transition metal chalcogenide, which is composed of S–Mo–S layers vertically stacked *via* weak van der Waals attraction.[1] Owing to the characteristics of high theoretical capacity and electrochemical activity, relatively large and easily expanded interlayer distance, easy preparation, and low cost, MoS_2 has been extensively investigated in the field of supercapacitors, batteries and electrocatalysts.[2–7] However, MoS_2 usually suffers from serious stacking and agglomeration problems during the preparation process, which leads to formation of many inaccessible active sites.[8] As a pseudocapacitive electrode material of supercapacitors, the low conductivity and large volume variation during repeated charge/discharge cycles also give rise to inferior rate capability and cycling stability of MoS_2, which restrains its practical application in energy storage.[9] Therefore, much efforts are devoted to ameliorating the capacitive performances of MoS_2.

To address the aforementioned drawbacks, endowing MoS_2 with various kinds of nanostructures can improve its electrochemical performances. The nanostructure design can effectively avoid the stacking and agglomeration problems of MoS_2 and expose more electroactive sites, which is beneficial to increasing the contact area with electrolyte ions. For instance, Kesavan *et al.* synthesized MoS_2 nanosheets *via* topochemical sulfurization, which revealed a high capacitance of 119.38 F g^{-1} and good cyclability of 95.1% over 2000 cycles.[10] Wei *et al.* fabricated MoS_2 nanoflowers *via* adding sodium chloride, which displayed a high capacity of 1120 F g^{-1} at 0.5 A g^{-1} and 96% of capacitance retention after 2000 cycles.[11] Broadening the interlayer spacing of MoS_2 is also an effective method to enhance the rate capability and cycling stability, since large interlayer spacing can afford rapid diffusion transportation of electrolyte ions between MoS_2 bilayers. Wang *et al.* prepared MoS_2 micro flowers with an interlayer spacing of 0.94 nm by reactant conversion-intercalation strategy, which delivered a specific capacity of 246.8 F g^{-1} at 0.5 A g^{-1}.[12] Cai *et al.* fabricated PEDOT@MoS_2 composite with an interlayer spacing of 1.02 nm *via* electrochemical co-deposition method, which exhibited a high specific capacity of 4418 mF cm^{-2} at 2 mA cm^{-2} and 100% of capacitance retention after 10 000 cycles.[13] In addition, the usually synthesized MoS_2 is stable semiconducting phase (2H-MoS_2) with low conductivity, while metallic phase (1T-MoS_2) is thermodynamically metastable but reveals better conductivity and hydrophilicity than 2H-MoS_2.[14–16] Therefore, developing 1T phase dominated hybrid phase MoS_2 is the optimal strategy to ameliorate the electrochemical properties of MoS_2. For example, Li *et al.* prepared high purity MoS_2 nanosheets with 83.6% of 1T phase, which achieved a high capacitance of 392 F g^{-1} at 1 A g^{-1} and 83% of capacitance retention after 10 000 cycles.[17] Although some

[a]School of Materials and Chemical Engineering, Zhongyuan University of Technology, Zhengzhou 450007, China. E-mail: yunanli@zut.edu.cn; qq@zut.edu.cn

[b]Center for Advanced Materials Research, Henan Key Laboratory of Functional Salt Materials, Zhongyuan University of Technology, Zhengzhou 450007, China. E-mail: mlwzzu@163.com

† Electronic supplementary information (ESI) available. See DOI: https://doi.org/10.1039/d3ra04852g

progresses have been made in enhancing the electrochemical performances of MoS_2-based electrodes, however, the preparation process of MoS_2 usually requires a high hydrothermal reaction temperature (usually above 200 °C), and the specific capacity and rate capability of MoS_2-based electrodes is still unsatisfactory, it is urgent to develop simple and low temperature strategies to ameliorate the specific capacity and rate capability of MoS_2-based electrodes.

Inspired by the above literature, in this work, MoS_2 nanoflowers regulated by Li_2SO_4 (L-MoS_2) are successfully fabricated *via* intercalating solvated Li ions in a relatively low hydrothermal reaction temperature (180 °C). Under appropriate intercalation of Li_2SO_4, MoS_2 nanosheets could self-assemble to form L-MoS_2 nanoflowers with an interlayer spacing of 0.65 nm. Due to the large specific surface area (23.7 $m^2\ g^{-1}$) and high 1T phase content (77.5%), L-MoS_2 as supercapacitor electrode delivers a maximum specific capacitance of 356.7 F g^{-1} at 1 A g^{-1} and maintains 49.8% of initial capacity at 20 A g^{-1}. Moreover, the assembled L-MoS_2 symmetric supercapacitor (SSC) device displays an energy density of 6.5 W h kg^{-1} at 413 W kg^{-1} and 79.6% of capacitance retention after 3000 cycles.

2. Results and discussion

2.1. Characterization

In this work, L-MoS_2 nanoflowers were self-assembled from MoS_2 nanosheets by intercalating moderate amount of Li_2SO_4 and the detailed preparation process of L-MoS_2 nanoflowers is shown in the ESI.† The morphologies of the obtained samples were first observed by scanning electron microscope (SEM). When $Li_2SO_4\cdot H_2O$ was not added in the hydrothermal reaction, the obtained MoS_2 is composed of intersecting nanosheets with thickness about 20 nm and reveals an obvious stacking/agglomeration phenomenon, as illustrated in Fig. S1a and b.† When 0.64 g $Li_2SO_4\cdot H_2O$ was added in the hydrothermal reaction, the solvated Li ions carrying water molecules intercalated into the MoS_2 bilayers, broadening the interlayer spacing of MoS_2 and introducing negative charges on the MoS_2 nanosheets.[18] The strong electrostatic repulsive force between negative charges on adjacent MoS_2 nanosheets affects the growth of MoS_2 and induces the self-assembly of MoS_2 nanosheets to form L-MoS_2 nanoflowers. As present in Fig. 1, the SEM images of L-MoS_2 exhibit perfect nanoflowers-like architecture without distinct agglomeration phenomenon. According to the four-probe tests, the conductivity of L-MoS_2 powder is 0.15 S cm^{-1}, which is higher than that of MoS_2 powder (0.11 S cm^{-1}). It is noteworthy that the amount of $Li_2SO_4\cdot H_2O$ added manifests an obvious effect on the morphology of L-MoS_2. When the amount of $Li_2SO_4\cdot H_2O$ added was 0.32 g, the solvated Li ions intercalated into the MoS_2 bilayers, introducing fewer negative charges on the MoS_2 nanosheets. The relatively weak electrostatic repulsive force between negative charges on adjacent MoS_2 nanosheets only induces partial self-assembly of MoS_2 nanosheets to form nanoflowers, leading to the resultant L-MoS_2-2.5 still presents stacking/agglomeration due to interlayer van der Waals attraction, as verified by the SEM images in Fig. S1c and d.† When the amount of $Li_2SO_4\cdot H_2O$ added was 0.96 g, the solvated Li ions intercalated into the MoS_2 bilayers, introducing more negative charges on the MoS_2 nanosheets. The stronger electrostatic repulsive force between negative charges on adjacent MoS_2 nanosheets induces the disorderly growth of MoS_2 nanosheets, which inevitably leads to the local collapse and agglomeration of the obtained L-MoS_2-7.5, as proved by the SEM images in Fig. S1e and f.†

The micro morphology of the samples was further observed by transmission electron microscope (TEM) tests. The TEM image in Fig. 2a further affirms that L-MoS_2 is self-assembled from thin and porous MoS_2 nanosheets. The high-resolution TEM (HRTEM) image in Fig. 2b exhibits an interlayer spacing of 0.65 nm, assigning to the (002) plane of 2H-MoS_2. Furthermore, the discontinuous lattice fringes marked within the dotted circles in Fig. 2b demonstrate the existence of abundant defects, which could be originated from the intercalation of Li ions. The TEM images of MoS_2 are shown in Fig. S2.† It can be seen that the interlayer spacing of (002) plane for MoS_2 is 0.64 nm. The high-angle annular dark-field scanning TEM (HAADF-STEM) image and the corresponding element mapping images in Fig. 2c confirm the homogenous distribution of Mo and S elements in L-MoS_2.

The crystallinity of L-MoS_2 and MoS_2 was analyzed by X-ray diffractometer (XRD). In Fig. 3a, L-MoS_2 and MoS_2 display identical diffraction peaks around 2θ of 13.5°, 32.5°, 35.7° and 57.4°, which can be respectively corresponded to the (002),

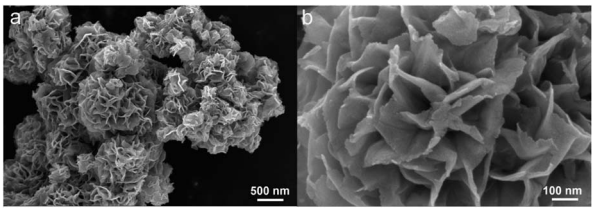

Fig. 1 SEM images of L-MoS_2 nanoflowers (a and b).

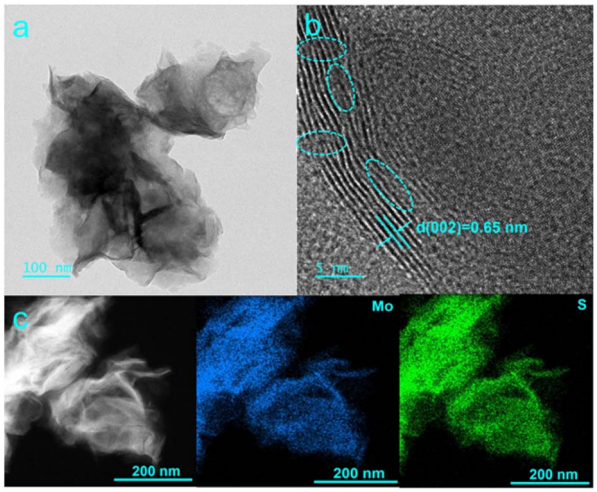

Fig. 2 (a) TEM, (b) HRTEM, (c) HAADF-STEM and corresponding element mapping images of L-MoS_2 nanoflowers.

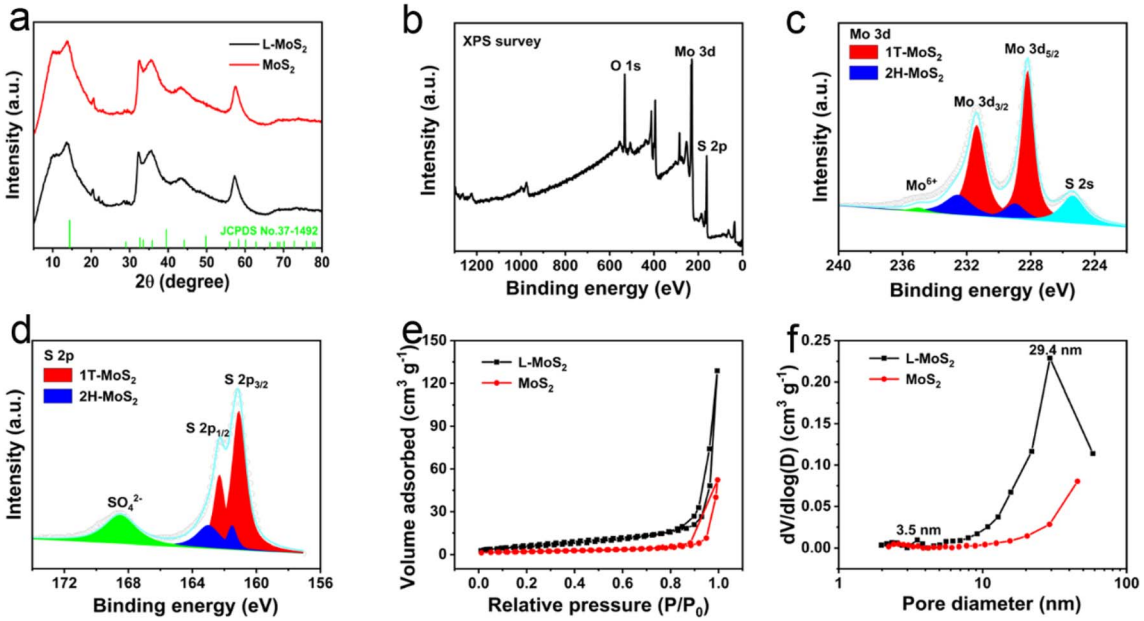

Fig. 3 (a) XRD patterns of L-MoS_2 and MoS_2. (b) The XPS survey spectrum of L-MoS_2. The high-resolution (c) Mo 3d, and (d) S 2p XPS spectrum of L-MoS_2. (e) N_2 adsorption–desorption isotherm curves of L-MoS_2 and MoS_2. (f) Pore size distribution curves of L-MoS_2 and MoS_2.

(100), (102) and (110) planes of 2H-MoS_2 (JCPDS no. 37-1492),[19] indicating that the intercalation of solvated Li ions has no distinct effect on the crystallinity of MoS_2. According to the Bragg equation, the (002) plane interlayer spacing of L-MoS_2 and MoS_2 is respectively calculated to be 6.48 and 6.34 Å, which are in line with the HRTEM results. In addition, the XRD patterns in Fig. S3† reveal that the (002) plane interlayer spacing of L-MoS_2-2.5 and L-MoS_2-7.5 is calculated to be 6.42 and 6.53 Å, respectively, further indicating that the intercalation of MoS_2 with Li_2SO_4 could broaden the interlayer spacing of MoS_2. The large interlayer spacing of MoS_2 can afford rapid electrolyte ions transportation in MoS_2, contributing to improve the rate capability to a certain extent.

X-ray photoelectron spectroscopy (XPS) tests were carried out to identify the chemical states of the samples. The presence of O, Mo, and S elements in L-MoS_2 is demonstrated by the XPS survey spectrum in Fig. 3b. Moreover, the trace amount of Li element in L-MoS_2 can be identified by the high-resolution Li 1s XPS spectrum illustrated in Fig. S4.† The high-resolution Mo 3d spectrum in Fig. 3c displays two peaks at 229.1 eV and 232.7 eV referring to the Mo^{4+} $3d_{5/2}$ and Mo^{4+} $3d_{3/2}$ of 2H-MoS_2, while the two peaks located at 228.4 eV and 231.6 eV corresponding to the Mo^{4+} $3d_{5/2}$ and Mo^{4+} $3d_{3/2}$ of 1T-MoS_2.[20] The weak peak at 235.1 eV demonstrates the presence of Mo^{6+} state, which is likely associated with the oxidation of MoS_2.[21] The S 2s peak at 225.6 eV is related to the Mo–S bond.[22] Based on the integral area of the deconvoluted Mo 3d spectrum, the content of 1T phase in L-MoS_2 is calculated to be 77.5%. The high-resolution S 2p spectrum in Fig. 3d reveals two peaks at 161.5 eV and 163.0 eV respectively assigns to S $2p_{3/2}$ and S $2p_{1/2}$ of 2H-MoS_2, while the peak located at 161.1 eV and 162.3 eV could be respectively referred to S $2p_{3/2}$ and S $2p_{1/2}$ of 1T-MoS_2.[20,23] The strong SO_4^{2-} peak at 168.5 eV could be possibly attributed to oxidation of MoS_2.[24] In addition, the two peaks of O 1s spectrum for L-MoS_2 at 531.5 and 532.8 eV shown in Fig. S4† could be respectively associated with O–Mo bond and adsorbed water.[25] The high-resolution Mo 3d and S 2p spectra of MoS_2 are illustrated in Fig. S4† and the content of 1T phase in MoS_2 is calculated to be 67.5%. It can be concluded that the intercalation of MoS_2 with solvated Li ions is conducive to increasing the content of 1T phase in MoS_2, which could be originated from that the negative charges on MoS_2 nanosheets lead to lowered formation energy of 1T phase.[18]

The porous architecture of L-MoS_2 and MoS_2 was investigated by N_2 absorption/desorption tests. In Fig. 3e, L-MoS_2 and MoS_2 exhibit a type-IV isotherm with an obvious hysteresis loop at high relative pressures, verifying the existence of mesopores.[26] The specific surface area of L-MoS_2 and MoS_2 is calculated to be 23.7 and 7.5 $m^2\ g^{-1}$, respectively. Compared with MoS_2, the pore size distribution curve of L-MoS_2 in Fig. 3f exhibits a bimodal pore size distribution. The narrow distribution centered at 3.5 nm might be related to the pores on the MoS_2 nanosheets, whereas the wide distribution centered at 29.4 nm could be ascribed to the void space formed by the self-assemble of MoS_2 nanosheets.[6] Therefore, the large specific surface area and bimodal pore size distribution are beneficial to increasing the contact area with electrolyte ions and affording fast ions transportation, and then ameliorating the specific capacitance and rate capability of L-MoS_2.[20,27]

2.2. Electrochemical performance

The electrochemical performances of L-MoS_2 and MoS_2 as supercapacitor electrodes were firstly studied in three-electrode system using 2 M KOH as electrolyte. In this work, nickel foam

was used as a current collector due to its high conductivity and porosity. After applying L-MoS_2 powder and MoS_2 powder to nickel foam, the conductivity of obtained L-MoS_2 and MoS_2 electrode is 0.96 kS cm^{-1} and 0.82 kS cm^{-1}, respectively. The cyclic voltammetry (CV) and galvanostatic charge–discharge (GCD) curves of nickel foam alone are illustrated in Fig. S5.† According to the CV and GCD test results, the contribution of foam nickel to capacitance could be negligible. The CV curves of L-MoS_2 and MoS_2 are compared at a scan rate of 20 mV s^{-1}, as present in Fig. 4a. It can be observed that both L-MoS_2 and MoS_2 reveal a anodic peak at 0.52 V and cathodic peak at 0.28 V, manifesting the pseudocapacitive nature of L-MoS_2 and MoS_2.[28] Moreover, L-MoS_2 exhibits a larger integral area of CV curve than that of MoS_2 at the same scan rate, signifying the higher specific capacitance of L-MoS_2. Fig. 4b shows the CV curves of L-MoS_2 at different scan rates. Obviously, all the CV curves display a pair of distinct redox peaks and the anodic peaks and cathodic peaks gradually move away mutually as the scan rate increases, which may be associated with the polarization phenomenon and internal resistance in L-MoS_2 electrode.[29] The GCD curves of L-MoS_2 and MoS_2 at a current density of 1 A g^{-1} are compared in Fig. 4c. The L-MoS_2 displays longer discharge time than that of MoS_2, further verifying the higher specific capacitance of L-MoS_2 after intercalating moderate amount of Li_2SO_4. All GCD curves in Fig. 4d are nearly symmetric, indicating that L-MoS_2 possesses a highly electrochemical reversibility.[30] The CV and GCD curves of MoS_2 reveal similar variation tendency with L-MoS_2, as illustrated in Fig. S6.† The specific capacitances of L-MoS_2 and MoS_2 calculated from the GCD curves are provided in Fig. 4e. It can be found that all the specific capacitances decrease with increasing the current density, which might be related to the limitation of K ions transportation at high current density.[31] At a current density of 1 A g^{-1}, L-MoS_2 achieves a specific capacitance of 356.7 F g^{-1}, which is larger than that of MoS_2 (282.8 F g^{-1}). When the current density is 20 A g^{-1}, L-MoS_2 still maintains a specific capacitance of 177.7 F g^{-1}, exhibiting a favorable rate capability with 49.8% of capacitance retention, which is better than that of MoS_2 (35.6%). In addition, the intercalation amount of Li_2SO_4 has a significant effect on the electrochemical properties of L-MoS_2. As present in Fig. S7,† all the specific capacitances of L-MoS_2-2.5 and L-MoS_2-7.5 are inferior than that of L-MoS_2 under the same current density, which could be associated with the morphology and interlayer spacing of L-MoS_2. Compared with L-MoS_2, L-MoS_2-2.5 exhibits smaller layer spacing with obvious stacking/agglomeration, which is adverse for the transportation of electrolyte ions into L-MoS_2-2.5, resulting in lower specific capacitance than L-MoS_2. Although the interlayer spacing of L-MoS_2-7.5 is greater than that of L-MoS_2, the local collapse structure of L-MoS_2-7.5 and excessive Li ions between the L-MoS_2-7.5 bilayers can hinder the rapid transportation of electrolyte ions within it, leading to significantly lower specific capacitance than L-MoS_2. Electrochemical impedance spectroscopy (EIS) measurements were conducted to study the kinetics of L-MoS_2 and MoS_2. In Nyquist plot, the intercept value on the horizontal axis at high-frequency region corresponds to the equivalent series resistance (R_s) and the diameter of the semicircle represents the charge transfer resistance (R_{ct}).[32,33] In Fig. 4f, the R_s value of L-MoS_2 (0.73 Ω) is less than that of MoS_2 (0.85 Ω), implying that the intercalation of solvated Li ions contributes to the transportation of electrolyte ions in L-MoS_2. Moreover, no obvious semicircle can be found in Nyquist plots, indicating that R_{ct} is negligible and

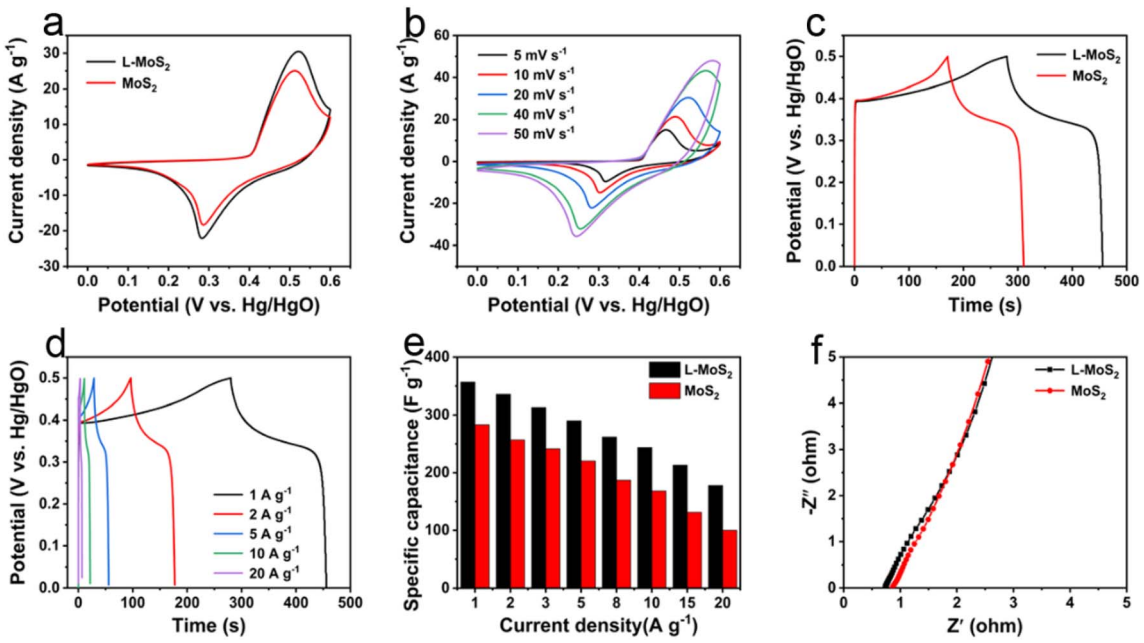

Fig. 4 Electrochemical performances of L-MoS_2 and MoS_2 electrodes in three-electrode system. (a) Comparative CV curves at a scan rate of 20 mV s^{-1}. (b) CV curves of L-MoS_2 electrode at different scan rates. (c) Comparative GCD curves at a current density of 1 A g^{-1}. (d) GCD curves of L-MoS_2 electrode at different current densities. (e) Specific capacitance *versus* current density curves. (f) Nyquist plots.

there is a fast electronic transfer during the redox reactions.[34] The cycling stability tests of L-MoS_2 and MoS_2 were carried out at a current density of 10 A g^{-1}. As present in Fig. S8,† L-MoS_2 maintains 76.5% of capacitance retention after 3000 cycles, which is higher than that of MoS_2 (48.8%), demonstrating a good cycling stability. The SEM images of L-MoS_2 electrode and MoS_2 electrode after 3000 cycles are illustrated in Fig. S9.† The MoS_2 electrode reveals a dense structure and appears several cracks. Moreover, MoS_2 losses its nanosheet structure and completely turns into nanoparticles after repeated charge/discharge cycles. In comparison, L-MoS_2 electrode still exhibits a loose and porous architecture after cycling, which is conducive to generating a good cycling stability. We summarize the electrochemical performances (specific capacitance, rate capability and cycling stability) of MoS_2-based electrodes in literature reports with our work. As shown in Table S1,† the electrochemical properties of L-MoS_2 are comparable to the previously reported literature.

Compared with MoS_2, L-MoS_2 displays superior specific capacitance, rate capability and cycling stability, which could be attributed to the following aspects. First, the self-assembled L-MoS_2 exhibits nanoflowers-like architecture with a large specific surface area of 23.7 m^2 g^{-1}, which can expose more electroactive sites and increase the contact area with electrolyte ions. Second, L-MoS_2 possesses an interlayer spacing of 0.65 nm, contributing to rapid transportation of electrolyte ions between L-MoS_2 bilayers. Finally, the high 1T phase content (77.5%) in L-MoS_2 is conducive to improving the conductivity and hydrophilicity, offering fast electronic transfer and large contact area with electrolyte ions.

In general, there are two charge storage mechanisms for MoS_2 electrode in KOH electrolyte, one is a diffusion-controlled process for intercalation/deintercalation of K^+ into/from the MoS_2 interlayers during the faradaic reaction, the other one is a capacitive process based on the surface adsorption/desorption of K^+ at the MoS_2 electrode/electrolyte interface, as shown in eqn (1) and (2):[9,27]

$$MoS_2 + K^+ + e^- \leftrightarrow MoS\text{-}SK^+ \quad (1)$$

$$(MoS_2)_{surface} + K^+ + e^- \leftrightarrow (MoS_2\text{-}K^+)_{surface} \quad (2)$$

The CV curves of L-MoS_2 and MoS_2 were analyzed by virtue of the method described in the ESI.† The calculated results shown in Fig. S10† manifest that the charge storage in L-MoS_2 comprises both diffusion-controlled process and capacitive process.[35] At low scan rate of 5 mV s^{-1}, the capacitive charge storage contribution ratio of L-MoS_2 is 39.0%, which is higher than that of MoS_2 (34.7%). Moreover, all the capacitive charge storage contribution ratios of L-MoS_2 are larger than MoS_2 at the same scan rate, further verifying the superiority of L-MoS_2. At 50 mV s^{-1}, the capacitive charge storage contribution ratio of L-MoS_2 accounts for 86.2%. Such a high capacitive charge storage contribution ratio is in favor of obtaining superior rate capability.[36]

To further evaluate the practical application of L-MoS_2 in supercapacitor, the SSC device was fabricated using two identical L-MoS_2 electrodes in 2 M KOH electrolyte. The CV curves of the SSC device in Fig. 5a reveal quasi-rectangular shape and keep the shape unchanged even at the high scan rate of 100 mV s^{-1}, demonstrating the superior capacitive behavior of the SSC device.[12] The GCD curves of the SSC device are shown in Fig. 5b. The quasi-triangular characteristic of GCD curves confirms a highly electrochemical reversibility of the ASC device. The specific capacitance of the SSC device is calculated from the GCD curves and illustrated in Fig. 5c. The SSC device could deliver a specific capacitance of 47.3 F g^{-1} at 0.8 A g^{-1} and 13.0 F g^{-1} at 5 A g^{-1}. Fig. 5d depicts the Nyquist plot of the SSC device, which displays a distinct semicircle at high frequency region. According to the equivalent circuit model shown in inset of Fig. 5d, the SSC device possesses a small R_s of 0.48 Ω and R_{ct} of 0.81 Ω, manifesting a low resistance and rapid charge transfer in the SSC device.[37] In Fig. 5e, the SSC device reveals 79.6% of capacitance retention and over 94% of coulombic efficiency after 3000 cycles at 2 A g^{-1}. The low coulombic efficiency could be due to the side reaction originated from the creation of transition metal and sulfur-containing nanocomposites with low reversibility.[19] The Ragone plot of the SSC device is shown in Fig. 5f. The SSC device exhibits a maximum energy density of 6.5 W h kg^{-1} at a power density of 413 W kg^{-1}, and keeps 1.8 W h kg^{-1} even at 3.2 kW kg^{-1}. The energy density and power density of L-MoS_2 SSC device are comparable to MoS_2-based SSCs in previously reported literature, such as 1T-MoS_2/Ti_3C_2 MXene (6.95 W h kg^{-1} at 239.48 W kg^{-1}),[16] MoS_2 nanosheets (6.56 W h kg^{-1} at 250 W kg^{-1}),[10] Cu doped MoS_2 (5.58 W h kg^{-1} at 299 W kg^{-1}),[38] and MoS_2–$Ti_3C_2T_x$ (5.1 W h kg^{-1} at 298 W kg^{-1}).[19] If the masses of nickel foam collector and polypropylene diaphragm are added, the actual energy of the SSC device is only 0.028 W h kg^{-1} at a power density of 1.8 W kg^{-1}. Therefore, MoS_2-based free-standing electrodes need to be developed to enhance the actual energy of the SSC device. Self-discharge and leakage current are extremely important parameters to evaluate the practical application of supercapacitors. The self-discharge and leakage current curves of the SSC device are illustrated in Fig. S11.† As shown in Fig. S11a,† the self-discharge of the SSC device could be ascribed to the following aspects. (i) The internal resistance (IR) drop that appears at the initial stage of self-discharge, which is associated with the charging current density and the electrolyte type.[39] (ii) The irreversible parasitic faradaic reaction could be originated from the surface oxygen-containing functional groups of L-MoS_2 electrode.[40] (iii) The charge redistribution caused by the inequality of charge distribution between the surface and inside of L-MoS_2 electrode.[41] According to the previously reported literature,[42] the studied self-discharge time of the SSC device is 10 h. The self-discharge rate could be measured by the open circuit voltage attenuation per unit time (OCV) and the OCV of the SSC device is 63.7 mV h^{-1}. In Fig. S11b,† as the current is stabilized, the leakage current of the SSC device is 46.5 μA (8.5 mA g^{-1}). If we do not consider the internal short circuit that may occur in assembling the SSC device, the leakage current of the SSC device is mainly derived from the parasitic Faraday reaction near the interfaces of L-

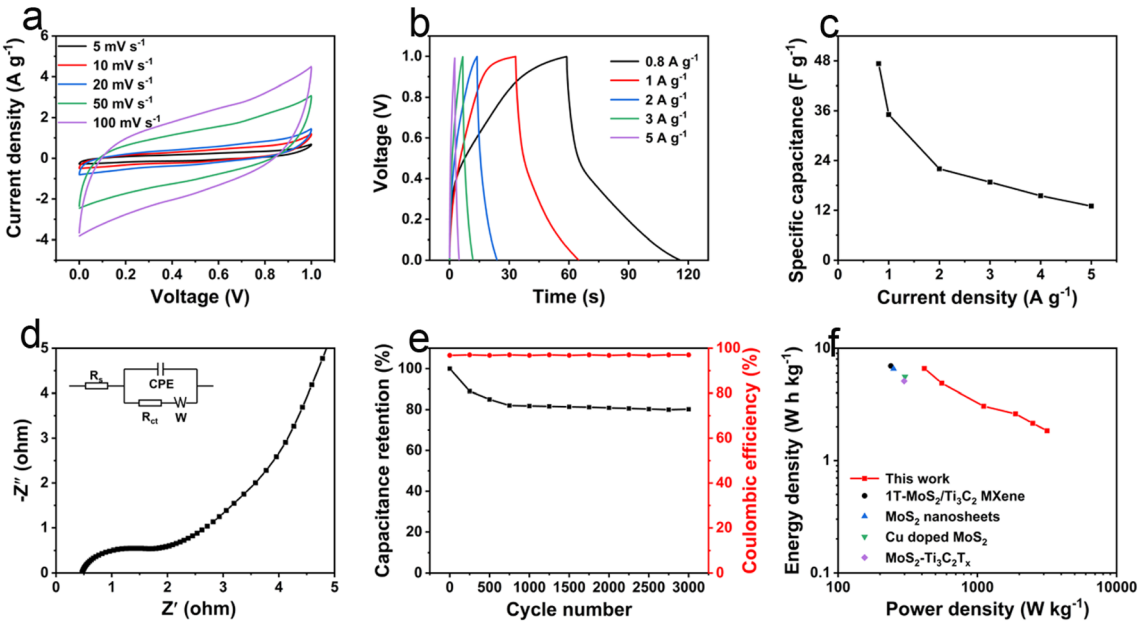

Fig. 5 Electrochemical performances of L-MoS_2 SSC in two-electrode system. (a) CV curves at different scan rates. (b) GCD curves under various current densities. (c) Specific capacitance *versus* current density curves. (d) Nyquist plot. Inset: the equivalent circuit model. (e) Cycling stability and coulombic efficiency after 3000 cycles at a current density of 2 A g^{-1}. (f) Ragone plot.

MoS_2 electrode and electrolyte caused by the surface oxygen-containing functional groups.[42]

3. Conclusions

In summary, L-MoS_2 nanoflowers with an interlayer spacing of 0.65 nm are successfully self-assembled from MoS_2 nanosheets under appropriate intercalation of Li_2SO_4. Due to the large specific surface area and high content of 1T-MoS_2, L-MoS_2 electrode delivers a maximum specific capacitance of 356.7 F g^{-1} at 1 A g^{-1} and keeps 49.8% of capacitance retention at 20 A g^{-1}. Moreover, the fabricated L-MoS_2 SSC device displays a highest energy density of 6.5 W h kg^{-1} and 79.6% of capacitance retention after 3000 cycles. It is believed that the intercalation of solvated Li ions could also be applicable to develop other 2D materials as advanced electrodes for supercapacitors.

Author contributions

Yunan Li: conceptualization, data curation, writing – original draft, writing – review & editing. Yang Sun: investigation, data curation. Sen Zhang: investigation, data curation. Xueling Wu: data curation. Meng Song: project administration. Mingli Jiao: funding acquisition. Qi Qin: writing – review & editing. Liwei Mi: funding acquisition, writing – review & editing.

Conflicts of interest

There are no conflicts to declare.

Acknowledgements

This work was supported by the National Natural Science Foundation of China (No. 21671205), the Program for Innovative Research Team (in Science and Technology) in University of Henan Province (No. 23IRTSTHN019), the Training Program for Young Backbone Teachers in Henan Colleges and Universities (No. 2021GGJS110), the Natural Science Foundation of Zhongyuan University of Technology (No. K2022MS005) and the Strength Enhancement Plan of Superior Disciplines of Zhongyuan University of Technology (No. SD202203). The authors would like to thank Gang Li and Jiaxiu Zhou from Shiyanjia Lab (https://www.shiyanjia.com/) for the SEM and TEM tests.

References

1 R. Hu, Y. Liao, H. Qiao, J. Li, K. Wang, Z. Huang and X. Qi, *Ceram. Int.*, 2022, **48**, 23498–23503.
2 S. W. Bokhari, A. V. Ellis, M. Uceda, S. Wei, M. Pope, S. Zhu, W. Gao and P. C. Sherrell, *J. Energy Storage*, 2022, **56**, 105935.
3 W. Jia, H. Wu, Y. Zheng, Z. Liu, G. Cai, J. Wen, G. Hu, T. Tang, X. Li, L. Jiang, Z. Wang, M. Li and H. Huang, *ACS Appl. Energy Mater.*, 2023, **6**, 2570–2581.
4 S. Li, C. Huang, L. Gao, Q. Shen, P. Li, X. Qu, L. Jiao and Y. Liu, *Angew. Chem., Int. Ed.*, 2022, **61**, e202211478.
5 J. Tian, C. Yang, R. Hao, F. Li, Z. Liu, W. Chen, Y. Lv and C. Lin, *Int. J. Hydrogen Energy*, 2022, **47**, 17871–17878.
6 X. Zhu, F. Xia, D. Liu, X. Xiang, J. Wu, J. Lei, J. Li, D. Qu and J. Liu, *Adv. Funct. Mater.*, 2023, **33**, 2207548.
7 M. K. Francis, K. Rajesh, P. B. Bhargav and N. Ahmed, *J. Mater. Sci.*, 2023, **58**, 4054–4069.
8 Z. Deng, H. Jiang and C. Li, *Small*, 2018, **14**, 1800148.

9 M. G. Fayed, S. Y. Attia, Y. F. Barakat, E. E. El-Shereafy, M. M. Rashad and S. G. Mohamed, *Sustainable Mater. Technol.*, 2021, **29**, e00306.
10 D. Kesavan, V. K. Mariappan, P. Pazhamalai, K. Krishnamoorthy and S. J. Kim, *J. Colloid Interface Sci.*, 2021, **584**, 714–722.
11 S. Wei, R. Zhou and G. Wang, *ACS Omega*, 2019, **4**, 15780–15788.
12 J. Wang, X. Zheng, Y. Dong, L. Chen, L. Chen and W. He, *Dalton Trans.*, 2023, **52**, 4537–4547.
13 Y. Cai, H. Kang, F. Jiang, L. Xu, Y. He, J. Xu, X. Duan, W. Zhou, X. Lu and Q. Xu, *Appl. Surf. Sci.*, 2021, **546**, 149088.
14 Z. Lei, J. Zhan, L. Tang, Y. Zhang and Y. Wang, *Adv. Energy Mater.*, 2018, **8**, 1703482.
15 F. Wan, X. Wang, C. Tang, C. Jiang, W. Wang, B. Li, Y. Zhang and X. Zhu, *J. Mater. Chem. A*, 2022, **10**, 12258–12268.
16 X. Wang, H. Li, H. Li, S. Lin, W. Ding, X. Zhu, Z. Sheng, H. Wang, X. Zhu and Y. Sun, *Adv. Funct. Mater.*, 2020, **30**, 0190302.
17 H. Li, H. Li, Z. Wu, L. Zhu, C. Li, S. Lin, X. Zhu and Y. Sun, *J. Mater. Sci. Technol.*, 2022, **123**, 34–40.
18 Z. Bo, X. Cheng, H. Yang, X. Guo, J. Yan, K. Cen, Z. Han and L. Dai, *Adv. Energy Mater.*, 2022, **12**, 2103394.
19 W. Hou, Y. Sun, Y. Zhang, T. Wang, L. Wu, Y. Du and W. Zhong, *J. Alloys Compd.*, 2021, **859**, 157797.
20 H. Niu, Z. Zou, Q. Wang, K. Zhu, K. Ye, G. Wang, D. Cao and J. Yan, *Chem. Eng. J.*, 2020, **399**, 125672.
21 Z. Wang, J. Wang, F. Wang, X. Zhang, X. He, S. Liu, Z. Zhang, Z. Zhang and X. Wang, *J. Alloys Compd.*, 2023, **947**, 169505.
22 P. Kour, Deeksha and K. Yadav, *J. Alloys Compd.*, 2022, **922**, 166194.
23 S. Li, Y. Liu, X. Zhao, K. Cui, Q. Shen, P. Li, X. Qu and L. Jiao, *Angew. Chem., Int. Ed.*, 2021, **60**, 20286–20293.
24 Q. Zhang, Y. Song, B. Chen, X. Hu, W. Peng, Y. Li, F. Zhang and X. Fan, *Chem. Eng. J.*, 2023, **454**, 140330.
25 X. Gu, L. Zhang, X. Ma, J. Wang, X. Shang, Z. Wang, M. Kandawa-Schulz, W. Song and Y. Wang, *Ionics*, 2022, **28**, 2337–2347.
26 I. T. Bello, K. O. Otun, G. Nyongombe, O. Adedokun, G. L. Kabongo and M. S. Dhlamini, *Int. J. Energy Res.*, 2022, **46**, 8908–8918.
27 K. B. Pisal, B. M. Babar, S. H. Mujawar, S. S. Mali, C. K. Hong, S. D. Sartale and L. D. Kadam, *Int. J. Energy Res.*, 2022, **46**, 18312–18327.
28 N. Joseph, P. Muhammed Shafi and A. Chandra Bose, *New J. Chem.*, 2018, **42**, 12082–12090.
29 Y. Yao, J. Wang, X. Ban, C. Chen, Q. Wang, K. Zhu, K. Ye, G. Wang, D. Cao and J. Yan, *EcoMat*, 2023, **5**, e12287.
30 S. Liu, Y. Yin, M. Wu, K. S. Hui, K. N. Hui, C.-Y. Ouyang and S. C. Jun, *Small*, 2019, **15**, 1803984.
31 K. Le, X. Zhang, Q. Zhao, Y. Liu, P. Yi, S. Xu and W. Liu, *ACS Appl. Mater. Interfaces*, 2021, **13**, 44427–44439.
32 M. Rashidi and F. Ghasemi, *Electrochim. Acta*, 2022, **435**, 141379.
33 H. Wu, Z. Guo, M. Li, G. Hu, T. Tang, J. Wen, X. Li and H. Huang, *Electrochim. Acta*, 2021, **370**, 137758.
34 S. Liu, Y. Yin, D. Ni, K. S. Hui, K. N. Hui, S. Lee, C.-Y. Ouyang and S. C. Jun, *Energy Storage Mater.*, 2019, **19**, 186–196.
35 M. S. Javed, X. Zhang, S. Ali, A. Mateen, M. Idrees, M. Sajjad, S. Batool, A. Ahmad, M. Imran, T. Najam and W. Han, *Nano Energy*, 2022, **101**, 107624.
36 Z. Tang, J. Dai, W. Wei, Z. Gao, Z. Liang, C. Wu, B. Zeng, Y. Xu, G. Chen, W. Luo, C. Yuan and L. Dai, *Adv. Sci.*, 2022, **9**, 2201685.
37 X. Sun, Y. a. Pang, S. Li, Y. Yu, X. Ding, L. Wang and Q. Zhang, *Ceram. Int.*, 2022, **48**, 21317–21326.
38 D. Vikraman, S. Hussain, K. Karuppasamy, A. Kathalingam, E.-B. Jo, A. Sanmugam, J. Jung and H.-S. Kim, *J. Alloys Compd.*, 2022, **893**, 162271.
39 S. Pu, Z. Wang, Y. Xie, J. Fan, Z. Xu, Y. Wang, H. He, X. Zhang, W. Yang and H. Zhang, *Adv. Funct. Mater.*, 2022, **33**, 2208715.
40 M. Haque, Q. Li, A. D. Smith, V. Kuzmenko, P. Rudquist, P. Lundgren and P. Enoksson, *J. Power Sources*, 2020, **453**, 227897.
41 W. Shang, W. Yu, X. Xiao, Y. Ma, Y. He, Z. Zhao and P. Tan, *Adv. Powder Mater.*, 2023, **2**, 100075.
42 W. Li, X. Yang, Z. Chen, T. Lv, X. Wang and J. Qiu, *Carbon*, 2022, **196**, 136–145.